RSC Advances

PAPER

View Article Online
View Journal | View Issue

Cite this: *RSC Adv.*, 2014, **4**, 31799

Optical and photocatalytic behaviours of nanoparticles in the Ti–Zn–O binary system†

Josephine B. M. Goodall,[a] Suela Kellici,[b] Derek Illsley,[c] Robert Lines,[c] Jonathan C. Knowles[de] and Jawwad A. Darr*[a]

Received 3rd June 2014
Accepted 23rd June 2014

DOI: 10.1039/c3ra48030e

www.rsc.org/advances

Continuous hydrothermal flow synthesis (CHFS) has been used as a rapid and clean, synthetic method to produce a range of crystalline nanoparticles in the Ti–Zn–O binary system. The nanopowders were prepared from aqueous solutions of titanium(IV) bis(ammonium lactato)dihydroxide (TIBALD) and hydrated zinc nitrate, respectively, using a CHFS reactor which uses superheated water (at 400 °C and 24.1 MPa) as a reagent and crystallizing medium. The resulting nanopowders were heat-treated at 850 °C for five hours in air to give photoactive semiconductor mixtures of rutile and zinc oxide and/or zinc titanates. The as-prepared powders and their corresponding heat-treated mixed phase photocatalysts were characterized using powder X-ray synchrotron diffraction, transmission electron microscopy, BET surface area measurement, X-ray photoelectron spectroscopy and UV-Vis spectrophotometry. Because of the interest for these materials in UVA and UVB attenuating materials, the UV-Vis profiles of the nanocomposites and solid solutions were studied. Photocatalytic activity of the samples towards the decolourisation of methylene blue dye was also assessed.

1. Introduction

A wide range of interesting optoelectronic properties such as good optical transparency and strong UV absorption have been exhibited by zinc oxide (ZnO) and titanium dioxide (TiO_2) materials. These materials have also attracted interest as either homo or heterometallic systems for use in a broad range of applications including photocatalysis[1,2] and UV-attenuating cosmetic sunscreens.[3,4] Both metal oxides are intrinsic wide bandgap semiconductors with an absorption band in the UV region.[5] TiO_2 (anatase structure) with a bandgap of 3.2 eV[6] tends to have higher photocatalytic activity for certain reactions,[7] whereas ZnO with a bandgap of 3.4 eV[6] tends to have a higher UVA absorption. Pure forms of ZnO or TiO_2 are generally limited as photocatalysts due to fast recombination rate of photogenerated electron–hole pairs. Combining the high UVA absorption ability of ZnO with the high photoactivity of titania, whilst enhancing charge separation and suppressing the recombination of photogenerated charge carriers has been the focus of considerable research efforts.[2,9–11] In particular, the intimate mixtures in the Ti–Zn–O binary system would be expected to give rise to broader UV absorption in comparison to pure ZnO and TiO_2 materials alone.[12] Considerable interest in this field has also focused on zinc titanate phases or their mixtures such as zinc orthotitanate, ZOT, (Zn_2TiO_4), zinc metatitanate, ZMT, ($ZnTiO_3$) and $Zn_2Ti_3O_8$, which has been reported as the low temperature form of ZMT. Such materials have found uses such as sorbants for removing sulphur,[13] as catalysts, as pigments, as microwave dielectrics, as electroceramics and as photoluminescent materials.[14] They are also of interest as low temperature co-fired ceramic (LTCC) materials, as a sintering temperature of below 1150 °C can often be achieved.[15] Zinc titanates are normally made *via* solid state processes with appropriate mixtures of ZnO and TiO_2. For example, Zn_2TiO_4 can be made *via* heat-treatment of a 2 : 1 molar mixture of ZnO and TiO_2 at temperatures in the range 800–1100 °C.[15]

The method of synthesis for mixed phase ceramic composites greatly affects particle characteristics including shape, size, intimacy of mixing and surface area and hence their bulk optical and other properties. A range of methods and structures have been investigated in the Ti–Zn–O binary system including zinc titanates,[14,16,17] Ti–Zn–O thin films,[18] composite layers of TiO_2 and ZnO,[19] and coupled semiconductors particles.[11] Conventional materials synthesis methods include CVD,[20] sol–gel techniques,[19] solid state techniques,[17] magnetron sputtering,[21] thermal oxidation,[22] thermal treatment of homometallic powders[23] and liquid phase routes.[24]

[a]*Department of Chemistry, University College London, 20 Gordon St, London, WC1H 0AJ, UK. E-mail: j.a.darr@ucl.ac.uk*

[b]*Department of Applied Sciences, London South Bank University, London SE1 0AA, UK*

[c]*Sun Chemical, Cray Avenue, St Mary Cray, Orpington, Kent, BR5 3TT, UK*

[d]*Division of Biomaterials and Tissue Engineering, UCL Eastman Dental Institute, 256 Gray's Inn Road, London, WC1X 8LD, UK*

[e]*WCU Research Centre of Nanobiomedical Science, Dankook University, San#29, Anseo-dong, Dongnam-gu, Cheonan-si, Chungnam, 330-714, South Korea*

† Electronic supplementary information (ESI) available: Powder XRD spectra, Raman spectra of Ti : Zn oxide mixtures, XPS spectra, UV-Vis absorption spectra of the heat-treated samples, STA profile for selected sample 8. See DOI: 10.1039/c3ra48030e

Many of the abovementioned synthetic procedures have drawbacks for example, due to multiple heating and grinding steps, solid state methods[17] can be energy and time intensive and do not directly offer well defined nanoparticle sizes. Batch hydrothermal methods are prone to batch to batch variations and do not offer similar product quality when scaled-up; magnetron sputtering methods[21] are difficult to scale-up and can only be carried out on small substrate samples rather than for powders. Sol–gel techniques[19] often require careful control over the reaction conditions, require special and costly precursors and use non-green solvents. Therefore, more efficient and controllable synthesis methods for nanomaterials production methods are of interest.

In contrast to more conventional nanomaterials syntheses, the use of continuous hydrothermal flow synthesis (CHFS) reactors represents a single step and controllable route for the rapid synthesis of nanoparticles and nano co-precipitates, giving materials with well-defined and desirable particle properties (such as small size, high surface area, size-dependent bandgap, high crystallinity, *etc.*) for a wide range of applications.[25–32] The typical CHFS process involves mixing a flow of superheated water (typically at ≤450 °C and 24.1 MPa) with an aqueous solution of metal ions (at room temperature), resulting in rapid hydrolysis and dehydration to give nanoparticles. Continuous hydrothermal reactions represent a very small (probably <1%) of the hydrothermal materials synthesis literature (the majority being batch reactions). Unlike batch hydrothermal reactions, where the nucleation of growth processes occur over several hours or days, in CHFS, the nucleation and growth processes due to the mixing in flow are in the order of seconds or fractions of a second, and indeed, the time from precursor to recovered nanoparticle (at the exit of the process) is in the order of a couple of minutes typically. Moreover, the reaction temperature when the two flows are mixed is typically in the range of 300–380 °C,[33,34] compared to typically less than 250 °C for batch hydrothermal processes. CHFS processes are also readily scalable with little or no effect on particle properties[33,34] and can also be used for combinatorial materials production,[35] which is very different to more conventional batch hydrothermal processes.

CHFS has been previously used for the synthesis of homometallic zinc oxide[36,37] and titania[30,38,39] nanoparticles. In addition, Ti–Zn–O composite mixtures have been also made using two reactors in series for sequential precipitation of TiO_2 on ZnO and *vice versa*.[40] CHFS has also been used to produce intimately mixed precursor co-precipitates which can be heat-treated in single step to form 'hard to make' heterometallic oxides.[29] Such materials may normally require multiple steps and involve prolonged synthesis using conventional methods. CHFS has also been used to directly make solid solutions in Zn–Ce oxide binary system, showing unprecedented solubility of Zn in CeO_2 phase.[41] It is reported that the formation of metal oxides in supercritical water proceeds *via* hydrolysis of the metal salts (ML_x) followed by the formation of hydroxides according to the following chemical reactions:

$$\text{Hydrolysis: } ML_x + xH_2O \rightarrow M(OH)_x + xHL$$

$$\text{Dehydration: } M(OH)_x \rightarrow MO_{x/2} + x/2H_2O$$

Herein, we report the synthesis of different phase mixtures directly from Ti^{4+} and Zn^{2+} salts using a CHFS system, and their optical and photocatalytic properties. CHFS provides a novel route to solid solutions or intimate mixtures of nano-titania and zinc oxide. The products were investigated using powder X-ray diffraction (XRD), X-ray photoelectron spectroscopy (XPS), transmission electron microscopy (TEM) and Brunauer–Emmett–Teller (BET) surface area measurements (N_2 adsorption). The optical properties of the powders were analysed using photoluminescence measurements and UV-Vis spectrophotometry. Finally, photocatalytic testing was performed in order to assess the decolourisation of methylene blue.

2. Experimental section

2.1 Chemicals and materials

Titanium(IV) bis(ammonium lactato)dihydroxide solution $[CH_3CH(O)CO_2NH_4]_2Ti(OH)_2$, 50 wt% in water (TiBALD) and zinc nitrate hexahydrate $[Zn(NO_3)_2 \cdot 6H_2O$, technical grade, >98%] were obtained from Sigma-Aldrich Chemical Company (Dorset, UK). Methylene blue (>96%) (MB) was obtained from Fisher (Loughborough, UK) and potassium hydroxide (KOH, analytical grade) was obtained from Merck, (Frankfurt, Germany). All experiments were conducted using deionised water (>10 MΩ).

2.2 Synthesis

All samples were made using a CHFS reactor (Fig. 1), the basic design of which has been reported elsewhere.[25,28–30] Briefly, it consists of three Gilson model 305 HPLC pumps including a H_2O pump, P1, a metal salt solution pump, P2, and a base

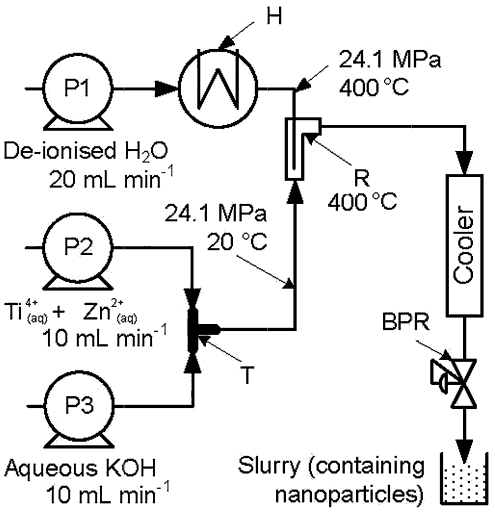

Fig. 1 Schematic representation of the three-pump continuous hydrothermal flow synthesis system that was used to prepare nanoparticles. Key: P = pump, H = heater, R = counter current mixer, BPR = back-pressure regulator T = 'T' piece mixer.

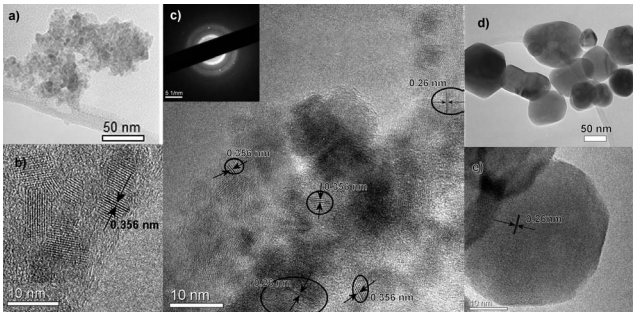

Fig. 2 (a) TEM image of sample 1 (bar = 50 nm), (b) HR-TEM image of sample 1 (bar = 10 nm), (c) HR-TEM sample of sample 8 inset SAED pattern (bar = 10 nm), (d) TEM image of sample 13 (bar = 50 nm), (e) HR-TEM image of sample 13 (bar = 10 nm).

solution pump, P3, an in-house built 2.5 kW electrically powered water preheater ("H" in Fig. 1), a counter-current mixing point ("R" in Fig. 1), an external long vertical water cooled pipe ("Cooler" in Fig. 1) and a back pressure regulator ("BPR" in Fig. 1, Tescom model 26-1762-24) fitted at the system outlet. The reactor, tubing and the fittings were all made of 1/8 in. 316 stainless steel (Swagelok) fittings and tubing, except the counter-current mixing point ("R" in Fig. 1) and 2.5 kW electrically powered water preheater, which were built from 1/4 in. fittings. Flow rates of 20, 10 and 10 mL min^{-1} were used for the superheated water feed, the mixed ion feed and the base feed, respectively. H_2O was pumped through the electrical preheating coil (2.5 kW) and heated to 400 °C.

In a typical experiment, each pre-made aqueous solution of TiBALD and zinc nitrate (with a total metal ion concentration of 0.2 M) was pumped to meet an aqueous flow of KOH base solution (0.2 M, also at room temperature) at a 'T' piece (Fig. 1). This mixture was then brought into contact with the flow of superheated water (at 400 °C and 24.1 MPa) inside an in-house built counter-current mixer ('R' in Fig. 1), whereupon the nanoparticles were produced in a continuous manner. The aqueous nanoparticle slurry was cooled in-line *via* an external long vertical water cooled pipe ("Cooler" in Fig. 1) and then continuously collected at the exit of the BPR (see Fig. 1). Nanoparticle slurries collected from the exit of the back-pressure regulator were cleaned up *via* centrifugation (Model Sigma 4k-15) at 5100 rpm for 20 min. The supernatant was removed (*ca.* 40 mL) and replaced with 40 mL of clean deionised water. The solids were then redispersed in water using a vortex mixer (VWR model VM-3000, Leicestershire, UK) on its maximum setting for 2 min and were further ultrasonicated for 5 min (30 W ultrasonic bath VWR USC100T). Each tube was further centrifuged at 5100 rpm for 30 min. This cleaning procedure was repeated twice with a final removal of 40 mL of liquid. The wet concentrated solids were freeze-dried for 22 h at 1.3×10^{-7} MPa. Based on the mass of dry powder, the yield was calculated to be in the range 82 to 92% for all the samples.

The precursor solutions were prepared to produce a desired Ti : Zn atomic ratios from 100 : 0 increasing in increments of 10 up to 0 : 100 (Table 1). Two additional samples were synthesised with atomic ratios of 75 : 25 and 25 : 75. Initial experiments suggested that the high Zn content samples often were highly deficient in the expected Zn content. Thus, samples from 30 : 70 to 10 : 90 Ti : Zn were synthesised with an excess of Zn^{2+} ions (5 mol%) in order to obtain the target Zn contents. Therefore, a nominal solution ratio of 25 : 75 for Ti : Zn was used to make the sample with a target final ratio of 30 : 70 in the nanopowder and 5 : 95 was used to make Ti : Zn target ratio of 10 : 90 in the product. Selected samples were also heat-treated at 850 °C for 5 h in air (ramp rates for heating and cooling were 10 °C min^{-1}) to investigate the formation of zinc titanates. These samples are identified with the letter "a" (*e.g.* 8a is the heat-treated sample 8 with nominal ratios of 40 : 60 Ti : Zn as shown in Table 1).

2.3 Equipment and techniques

Freeze-drying was performed on all samples using a Virtis Genesis 35XL freeze dryer. The wet slurries were frozen in liquid nitrogen and then freeze-dried for *ca.* 22 h at 1.3×10^{-7} MPa. The samples were then heat-treated at 850 °C for 5 h in air using a Carbolite CWF1300 furnace (using a heating and cooling rate

Table 1 The ratio of Ti^{4+} : Zn^{2+} in the precursor feed and the EDS atomic percent results

Sample	Desired ratio Ti : Zn	Used precursor ratio Ti : Zn	EDX Ti[a] (at %)	XPS Ti[a] (at %)
1	100 : 0	100 : 0	100.0	100
2	90 : 10	90 : 10	89.3	89.9
3	80 : 20	80 : 20	77.0	79.3
4	75 : 25	75 : 25	75.2	—
5	70 : 30	70 : 30	68.7	72.9
6	60 : 40	60 : 40	59.1	58.7
7	50 : 50	50 : 50	48.4	49.1
8	40 : 60	40 : 60	37.2	40.5
9	30 : 70[b]	25 : 75	29.9	29.9
10	25 : 75[b]	20 : 80	25.6	—
11	20 : 80[b]	15 : 85	21.0	19.97
12	10 : 90[b]	5 : 95	9.3	10.67
13	0 : 100	0 : 100	0.0	0

[a] With respect to the total metal ion content. [b] Samples made with and excess *ca.* 5 at% of Zn^{2+} ions in the precursor feed.

of 10 °C min^{-1}). Synchrotron XRD patterns were taken on the Diamond I11 beamline, as previously described by the authors (λ = 0.8269 Å).[42] Continuous scans were collected over the 2θ range 0–150° and the diffraction patterns are shown over a 2θ range of 10–45°. A Brüker D8 Advance diffractometer with a Ni filtered Cu–K radiation ($\lambda = 1.54$) Å and a Lynx Eye detector was used for an *in situ* (XRD) study of the phase behaviour of sample '8' (40 : 60 for Ti : Zn) with temperature. An Anton Paar HTK16 heating stage with an Anton Paar TCU 2000 control unit was used, integrated with the Brüker control software. The as-precipitated nanopowder was placed on a platinum heater stage. Heating temperature was observed using an R-type thermocouple welded to the bottom of the platinum heater strip (temperature accuracy ±1 K). After sealing, the platinum heater enclosure was purged with air at a 2 mL min^{-1} flow rate. The sample was heated at 10 °C min^{-1} up to 1200 °C. Data was collected over 2θ ranges of 23–40° and with a step size of 0.02 and a count time of 0.1 s. Thermal gravimetric analysis was carried out in order to study thermal behaviour of sample 8 (40 : 60 for Ti : Zn) under heating using a Setaram combined TG-DTA in the range 20 to 1150 °C at a heating rate of 10 °C min^{-1} in air.

Particle size and morphology of selected as-prepared nanopowders were investigated using a HR-TEM model JEOL 4000EX high resolution transmission electron microscope at Oxford University (400 kV accelerating voltage). Samples were collected on carbon-coated copper grids (Holey Carbon Film, 300 mesh Cu, Agar Scientific, Essex, UK) after being briefly dispersed ultrasonically (Kerry™ Ultrasonic bath, Skipton, UK) in ethanol for 3 minutes. In addition, selected area diffraction patterns (SADP) were recorded in order to confirm the crystallinity of the powders. Particle size analysis was performed using Digital Micrograph™ (Gatan) particle size analysis software. Brunauer–Emmett–Teller (BET) surface area measurements were performed on a six station Micromeritics ASAP 2420 analyser (N_2 absorption). The powders were degassed at 200 °C in N_2 (purge gas supplied by BOC, UK) for 5 h, prior to BET analyses. These parameters were chosen as the degassing conditions after a time temperature assay for the CHFS as-prepared TiO_2 and ZnO nanopowders. The UV-Vis absorption spectra of the photocatalyst powders were measured using the diffuse reflectance method on a Perkin Elmer Lambda 950 instrument with an integrating sphere (Spectralon™ was used as a reference material). Additionally, the band-gaps were calculated using the Kubelka–Munk function (eqn (1)) *via* conversion of the reflectance spectra (R) for indirect and direct transitions.[43] Determination of bandgap values for pure TiO_2 and ZnO samples calculated using Kubelka–Munk function are shown in ESI section Fig. S9.†

$$F_{KM} = \frac{(1 - R^2)}{2R} \quad (1)$$

An Oxford Instruments Inca 400 calibrated EDX detector connected to a scanning electron microscope (JEOL 5410 LZSEM) was used to carry out the elemental analysis for all the samples. An average of 10 area scans was used for each measurement. The SEM was operated at 25 kV and all samples were carbon coated prior to measurement. X-ray photoelectron spectroscopy (XPS) experiments were performed on selected samples using a Kratos Axis Ultra-DLD photoelectron spectrometer using monochromatic Al-Kα radiation (photon energy 1486.6 eV, 150 W power). Survey scans were performed at pass energy (PE) of 160 eV, whilst detailed scans were performed at PE 40 eV. All data were analyzed using CasaXPS™ software (Version 2.3.14). Spectra were acquired using the Kratos immersion lens charge neutralisation system, and all spectra were subsequently calibrated to the C(1s) signal, which was assigned a value of 284.7 eV, and attributable to adventitious carbon. Curve fits were performed using a Shirley background and a Gaussian peak shape with 30% Lorentzian character.

2.4 Photocatalytic tests

A parallel photocatalytic reactor system was used, which is similar to the one described elsewhere by the authors.[44] It consisted of nine 50 mL glass beakers (Duran). The light source was a fan-cooled 400 W high-pressure Hg discharge lamp (400HPLR, Philips, RS Components). As reported previously,[44] the main light emissions measured using an Ocean Optics USB4000 spectrophotometer (Duiven, Netherlands) are at 365, 405, 436, 546, and 577 nm. The UV and visible illumination under the centre of a 4 mm thick frosted glass diffuser (Bow-Mirrors, Bow, London) was found to be 2.7 mW cm^{-2} (J-221 UV meter, Ultra Violet Products, Cambridge, UK) and 82 klx (HI97500 photometric light meter, Hanna Instruments, UK), respectively, showing that a much greater proportion of the output of the Hg discharge lamp is in the visible part of the spectrum. UV-Vis absorption spectra of the MB solution were recorded using an Ocean Optics USB 4000 spectrophotometer with a DH-2000-BAL deuterium halogen light source and 6 μm fibre optic cables. The photocatalytic activity of the nanopowders was evaluated by measuring the photo-decolourisation of aqueous MB dye under illumination and access to air. Adsorption coefficients were also determined using Langmuir–Hinshelwood model (see ESI data, Tables S2 and S3†). The pH of the methylene blue stock solution was measured as 6.8 using a pH meter (Malvern MV114-SC SEN0106).

For a photocatalytic test,[44] 0.01 g of relevant photocatalyst was suspended in standard MB solution (50 mL, 2.0×10^{-5} M) in each of the nine reactors. The mixtures were stirred for 30 minutes with a magnetic stirrer in the absence of light in order to allow the dye to reach an equilibrium adsorption on the catalyst surface. The samples were then irradiated with light and, at thirty minute intervals, the light was switched off and 5.0 mL aliquots were temporarily removed from each bulk suspension. These samples were briefly centrifuged (5 min at 5100 rpm), then the remaining dye was analysed *via* UV-Vis spectrophotometry by measuring the absorbance intensity at 664 nm. The quantitative determination of unreacted dye was calculated using a calibrated correlation between the measured absorbance and its concentration. In all experiments after the final measurement, the decoloured methylene blue was kept for 24 h in air in the dark to check that the dye had been degraded

and not simply reduced to the leuco form.[45] Methylene blue (MB) exhibit blue colour when it is in an oxidizing environment, but upon exposure to a reducing agent it goes colourless (leuco methylene blue). The direct degradation of methylene blue was measured as a control and the first order rate constant was calculated to be 4.1×10^{-5} s^{-1} which was an order of magnitude smaller than the least active sample.

3. Results and discussion

3.1 Nano Ti–Zn–O mixtures

In this work, Ti–Zn–O mixtures were synthesised in a continuous hydrothermal system which facilitated the rapid synthesis of nanoparticles from a 0.2 M (total concentration) pre-mixed aqueous solution of TiBALD and zinc nitrate under alkaline conditions. The concentration of the base (KOH) was set at 0.2 M in all cases. The individual metal salt solutions were first prepared manually to produce a desired Ti^{4+} : Zn^{2+} atomic ratio from 100 : 0 increasing in increments of 10 up to 0 : 100 (Table 1). All of the as-prepared Ti–Zn–O binary nanoparticle mixtures were in the form of white coloured or off-white aqueous slurry. In general, the higher the proportion of Ti^{4+} in the sample, the longer this suspension was stable in water without sedimentation (>2 days). For samples containing more Zn^{2+}, sedimentation occurred in as little as 30 min (*e.g.* 0 : 100). The samples were labelled from 1 to 13 in order of increasing Zn content where sample 1 was 100% TiO_2 and sample 13 was 100% ZnO (Table 1).

The nominal ratios of Ti^{4+} : Zn^{2+} in the precursors and the EDX metal analyses results for all binary mixtures are also summarized in Table 1. At high Ti^{4+} : Zn^{2+} ratios, the proportion of Ti to Zn in the solid was similar to the precursor ratio of the solution feed. At low Ti^{4+} : Zn^{2+} ratios, the sample had an excess of Ti compared the theoretical ratio for the corresponding feed. This could be due to the higher yield of pure TiO_2 (*ca.* 92%) compared with that of pure ZnO (*ca.* 82%) when made under similar conditions in the CHFS reactor. For the low Ti : Zn ratios, samples 9–12 were made with an excess of zinc to achieve the desired ratio in the solid sample as described in the Experimental section (see Table 1). The differences in the results obtained by XPS and EDX are largely due to the errors in each measurement and also because XPS is not able to penetrate into the materials which EDX is more representative of the bulk.

Fig. 2 shows the TEM and HR-TEM images for sample 1 (TiO_2), sample 8 (nominal Ti^{4+} : Zn^{2+} ratio of 40 : 60) and sample 13 (ZnO). Sample 1 (Fig. 2a and b) is characteristic of CHFS titania with an average crystallite size of 4.9 ± 1.2 nm (255 particles sampled) and an anatase (101) lattice spacing of 0.356 nm, which is in agreement with the literature value.[46] By contrast, the pure zinc oxide sample 13 (Fig. 2d and e) revealed particles with mean size of 66 ± 17 nm (150 particles sampled) and a polygonal morphology with the characteristic zinc oxide (0002) lattice spacing. As for sample 8, two distinct lattice spacings were observed, 0.36 and 0.26 nm that are thought to correspond to the (101) anatase spacing and the (0002) wurtzite lattice spacing, respectively (Fig. 2c).[47] The selected area electron diffraction pattern (inset Fig. 2c) suggests that sample 8 is a polycrystalline, intimate mixture of anatase and zinc oxide. In sample 8, the mean ZnO particle size from the areas of characteristic ZnO (0001) spacing is 22.6 ± 8.2 nm (100 particles sampled). This suggests that TiO_2 may be acting as a nucleating site for the ZnO particles during co-precipitation, which would lead to a reduction in the particle size of ZnO particles compared to those precipitated in the absence of any Ti^{4+} precursor.

Fig. 3 shows the high resolution PRXD data for all the freeze-dried and as-prepared samples collected at the synchrotron (except for sample 5 and sample 10, the XRD of which were collected using a standard PXRD laboratory equipment, see ESI section†). Notably, the data collected at the synchrotron (XRD wavelength was 0.826017 Å) appear at different 2θ values compared to PXRD data collected on a standard equipment as expected (due to the different incident wavelength used). Samples with high Ti : Zn ratios (from samples 1 to 6) were identified as having an anatase structure (JCPDS 21-1272) and samples with a lower Ti : Zn ratio (from sample 7 to 13) were indexed to the hexagonal closed packed wurtzite structure (JCPDS 36-1451).

Peaks corresponding to ZnO were first clearly identified in the mixture for sample 7 (nominally with 50 mol% Zn). Consequently with increasing Zn content, the anatase peaks became progressively weaker whilst the wurtzite peaks become relatively more intense. Samples 4, 5 and 6 have broader anatase peaks than samples with higher Ti content, indicating that they are less crystalline or have smaller crystallites. The former is possibly due to Zn atoms doping into the anatase structure leading to a more amorphous structure. All the samples have some anatase peaks (indicating *ca.* $2\theta = 25.6°$) except sample 13 which was pure ZnO. The presence of anatase was confirmed using Raman spectroscopy (see ESI data†) since anatase is a good Raman scatterer and this analytical technique exhibits higher anatase phase sensitivity in comparison to XRD. Zn^{2+} has a limited solubility in TiO_2 [48,49] and due to the atomic size mismatch, only a small amount of Zn^{2+} ions can normally

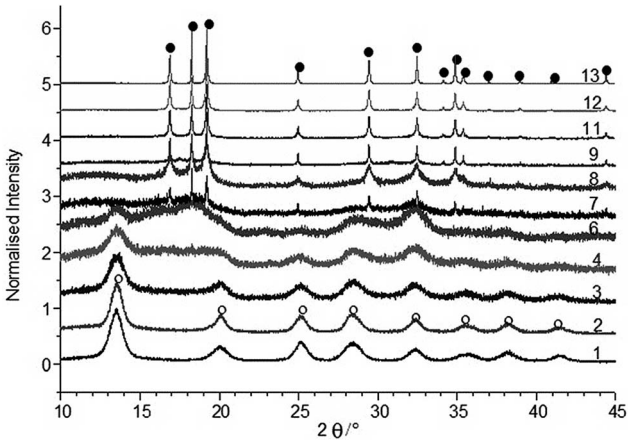

Fig. 3 Synchrotron XRD diffraction patterns of TiO_2 : ZnO nano-coprecipitates (○-anatase peaks, ●-ZnO peaks).

substitute onto the Ti lattice and therefore zinc ions tend to locate at discontinuities in TiO_2.[59]

In the literature, XRD peaks corresponding to ZnO have been observed in zinc doped titania between 10 and 20 mol% of dopant.[50,51] Herein, samples 1–4 containing up to 25 mol% Zn (with respect to Ti) showed no evidence of a separate ZnO phase in the diffraction pattern. The rapid crystallisation of CHFS has been found to extend the boundaries of solid solutions, and could also have extended the amount of Zn^{2+} in titania which would explain the broad peaks seen in the XRD for samples 4–6, which contains zinc in the titania lattice.

Fig. 4 shows the BET specific surface area (SSA) of the all the as-prepared samples are in the range 290 $m^2 g^{-1}$ (for sample 1, *i.e.* pure TiO_2) to *ca.* 30 $m^2 g^{-1}$ (for sample 13, *i.e.* pure ZnO). In general, for Ti–Zn oxide binary system (samples 1–13) a decrease of SSA with increasing zinc content is observed. The SSA remains high (270–299 $m^2 g^{-1}$) for samples 2–6 (*ca.* 10–40% Zn). For sample 7 (50 : 50) there is a marked reduction in the SSA to *ca.* 210 $m^2 g^{-1}$ which coincided with the first appearance of crystalline ZnO peaks in the corresponding XRD pattern (Fig. 3). This is expected, given that the size of ZnO particles (*ca.* 66 nm) synthesised in the CHFS system is larger than that of pure TiO_2 (*ca.* 4.9 nm). This suggests that the formation of larger ZnO particles resulted in the overall decrease in surface area. The surface area decreases from *ca.* 134 $m^2 g^{-1}$ to 30 $m^2 g^{-1}$ between samples 12 (10 : 90) and 13 (0 : 100) which is attributed to an increase in the size of ZnO when synthesised in the absence of titanium ions. The BET surface area did not appear to correspond to the peak broadening observed in the XRD patterns and specifically the broad peaks observed in samples 4, 5 and 6. There is no increase in BET surface area for these samples that could correspond to a decrease in the particle size. This supported that the peak broadening in the XRD data for samples 4–7 may be due to a decrease in crystallinity because of lattice strain induced by doping of Zn^{2+} ions into the titania lattice.

X-ray photoelectron spectroscopy (XPS) experiments were performed to investigate the concentration of the titanium and zinc in the lattice, their oxidation state and the effect on the structure (Fig. 5). Generally, the survey spectra for all samples exhibited strong peaks for titanium (with the exception of sample 13), oxygen and zinc (except in sample 1). Very small amounts of nitrogen were also found, the source of which we attribute to nitrogen incorporation/doping from the precursor itself.[30,39] Photocatalytic activities of N-doped nano-titanias have been previously studied and reported by authors.[51] XPS of sample 1 (nano-TiO_2 powder) was examined in order to assess the amount of Ti^{3+} *versus* Ti^{4+} ions.

The spectrum of the nano-TiO_2 has a Ti $2p_{3/2}$ binding energy of 458.6 eV, with a spin–orbit splitting of 5.7 eV (Fig. 5a), which is in excellent agreement with the values reported for Ti^{4+} in TiO_2 (NIST database).[52–54] The same sample also exhibited an O 1s peak at 529.9 eV (Fig. 5c), characteristic of the lattice oxide, a high binding energy shoulder was also observed at 530.9 eV which is ascribed to surface hydroxide groups.[52,55] The ratio of Ti : $O_{(lattice)}$ was found to be 1 : 1.9, thus, the XPS data together with the XRD data, suggests that the nano-TiO_2 material synthesized using the CHFS system is close to stoichiometric TiO_2 anatase.[30] XPS of sample 13 (pure nano-zinc oxide) has a Zn $2p_{3/2}$ binding energy of 1021.92 eV with a spin orbit coupling of 23 eV (Fig. 5b). The O1s peak for the ZnO samples was found to split into three peaks; a low energy peak at 529.9 eV, an intermediate energy peak at 531.5 eV, and a small high energy peak at 532.6 eV (Fig. 5d). The low energy peak was attributed to O^{2-} in the wurtzite lattice. The intermediate peak was attributed to O^{2-} in oxygen deficient areas and the high energy peak was due to chemi-adsorbed surface species such as hydroxyl groups.[56,57] The peak due to oxygen deficiencies has been reported in literature to be higher in intensity than the (bulk) lattice oxygen peak at the surface of ZnO.[58] The ratio of Ti^{4+} : Zn^{2+} from XPS was found to correspond well with the results obtained from EDX analysis and are shown in Table 1. The EDX and XPS atomic percentages of Ti, with respect to the total metal ion content are all within 5% of each other. This suggests that neither TiO_2 nor ZnO segregate appreciably to the surface of the

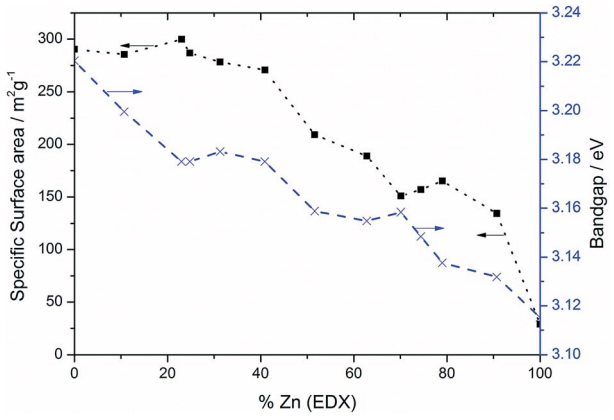

Fig. 4 The BET surface area (squares) of samples 1–13 with zinc content (samples degassed for 5 hours at 200 °C) and the calculated bandgaps (crosses) in eV.

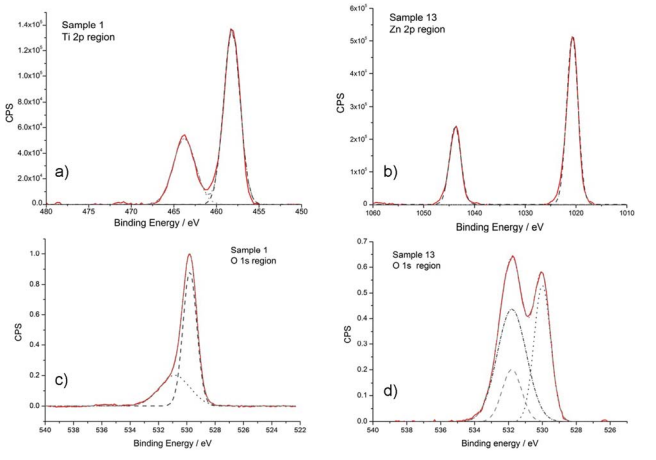

Fig. 5 The XPS spectra showing the (a) Ti 2p region, sample, (b) Zn 2p region of sample 13, (c) O1s region in sample 1, and (d) the O1s region of sample 13.

co-precipitates, and are intimately mixed throughout. The position of the Ti 2p and Zn 2p peaks did not shift with varying Ti : Zn ratio and no evidence of Ti^{3+} was found in any of the samples, supporting the XRD evidence that no zinc titanate phases were found in the as-prepared samples. The lattice O1s peak (529.8 ± 0.2 eV) did not shift with varying Ti : Zn ratio but the shoulder at 530.9 eV in sample 1, grew and shifted towards 531.5 eV (sample 13) with increasing zinc content. In titania, the peak at 531 eV is due to chemi-absorbed oxygen species such as hydroxyl groups. In ZnO, the peak at 531.4 eV is due to oxygen ions in regions of the lattice that are oxygen deficient such as the surface. A small shoulder emerges in the high zinc samples (samples 9–13) at 532.6 eV, which is thought to be due to species such as hydroxyl groups at the surface of the ZnO.

The optical properties of Ti–Zn samples were analysed using UV-Vis spectrophotometry and plots are shown in Fig. 6. The UV-Vis absorption profiles for the Ti–Zn–O binary mixtures revealed two main shapes. Firstly, a ZnO type profile with a steep absorption edge and a flat absorption above and below the bandgap (sample 13). Secondly, a TiO_2 type profile is observed where the bandgap transition is less steep and varies over a much wider wavelength range (sample 1). Samples with high Ti content (samples 2–6) were similar to the TiO_2 UV-Vis absorption profile, whereas the samples with lower Ti ratios (samples 8–12) tended to have the ZnO like UV-Vis absorption profile. Sample 7 (Ti : Zn 50 : 50) has some characteristics of both profiles. The optical badgaps (shown in Fig. 4) were determined herein from the absorption edges and using the Kubelka–Munk model for a direct and indirect transition for ZnO and TiO_2, respectively. The bandgap varied with the ratio of Ti : Zn between 3.22 eV which is the value for anatase titania (indirect transition), to 3.12 eV which is tending toward a bandgap of 400 nm for ZnO (direct transition). As samples 1–6 have an anatase type profile, an indirect transition was assumed for the determination of the bandgap. A direct transition was used for samples 8–13 which display a ZnO type absorption profile. The estimated bandgap of sample 7 was 3.18 eV with either a direct ($(F_{KM}h\nu)^2$ *vs.* $h\nu$) or indirect transition ($(F_{KM}h\nu)^{1/2}$ *vs.* $h\nu$) assumed for the calculation. In each case, the plot had a distinct linear region which indicated the absorption edge. The bandgap energy increases (blue shift) from sample 1 (3.22 eV) with decreasing Ti content to 3.25 eV for sample 6 (*ca.* 60 : 40). There is a slight reduction in the bandgap to 3.18 eV between samples 6 and 7 (*ca.* 50 : 50) and the bandgap then tended towards the ZnO value of 3.12 eV with further decrease in Ti content. This is thought to be due to an increase in the UVA absorption corresponding to the transition to a majority ZnO phase. The change between sample 6 and 7 could be due to a shift in the primary phase (from XRD) from anatase to zinc oxide.

3.2 Solid state synthesis of zinc titanates

Ti–Zn oxides nanopowders prepared using continuous hydrothermal flow synthesis (CHFS) reactor were used as nanoprecursors for the solid state synthesis of zinc titanates. The powders were heat-treated at 850 °C for five hours and were further analysed using synchroton and powder VT-XRD and STA. The letter "a" is added to indicate heat-treated sample. Fig. 7 shows the synchrotron powder XRD patterns of the heat-treated Ti–Zn samples. 1a (100 : 0 Ti : Zn) is entirely rutile phase as expected. The anatase to rutile transition for CHFS synthesised titania was found to start at 500 °C and be complete at 900 °C in samples heated for one hour and in STA analysis the transition was found to start at 610 °C.[30] Samples 2a–6a (10–40% Zn^{2+}) were found to be a mixture of rutile and $ZnTiO_3$ (zinc metatitante). No $Zn_2Ti_3O_8$ crystal phase was observed in the diffraction pattern which agrees with the literature, where samples were subject to heat-treatment at temperatures less than 820 °C to obtain $Zn_2Ti_3O_8$. It is not found to form on cooling from other phases.[13,59] Sample 7a was found to be a three phase mixture containing rutile, $ZnTiO_3$ and zinc

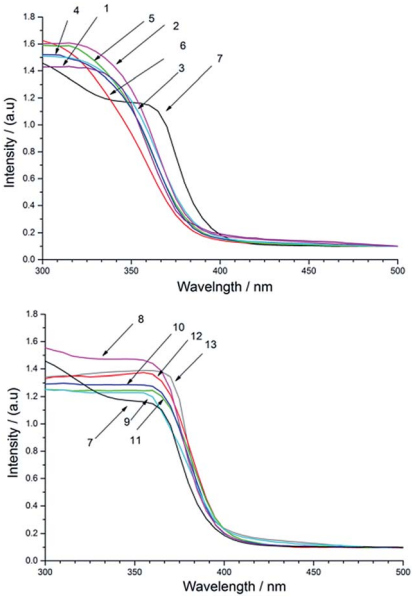

Fig. 6 The diffuse reflectance UV-Vis absorption profiles for as-prepared Ti–Zn–O binary nanopowder samples (a) 1–7 and (b) 7–13.

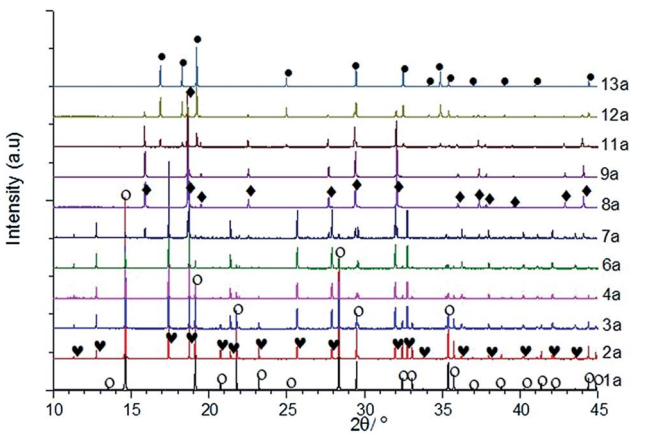

Fig. 7 Synchrotron X-ray diffraction patterns of 1a–13a (○ rutile, ♥ $ZnTiO_3$, ◆ Zn_2TiO_4, ● ZnO).

orthotitante, Zn_2TiO_4. It has been found that $ZnTiO_3$ is difficult to make directly from 1 : 1 mixtures of ZnO and TiO_2.[16] The phase mixture in sample could be due to initial formation of rutile from the anatase and then formation of Zn_2TiO_4 and $ZnTiO_3$ from the remaining sample which would then have a higher relative % of Zn. Sample 8a appeared (from the synchrotron XRD pattern) to be pure Zn_2TiO_4. For samples 9a–12a, a mixture of ZnO and Zn_2TiO_4 was seen. This is as expected from the phase diagram.[13,17] Sample 13a was pure ZnO. In the as-prepared samples 1–13, anatase was present in all but sample 13.

In the heat-treated samples, rutile is only present in samples with ≤50% Zn, which is likely due to the formation of titanates. At 850 °C from the phase diagram proposed by Dulin and Rase, at the higher Zn compositions (above sample 8a), no titania is expected to form.[17] It has been reported that $ZnTiO_3$ only forms in the presence of rutile, whereas Zn_2TiO_4 and $Zn_2Ti_3O_8$ are limited by anatase.[59] In this work $ZnTiO_3$, was made from an anatase starting material, however the anatase to rutile phase transformation is expected to start above *ca.* 600 °C so it would be expected that anatase may have transformed to rutile during heating, allowing the subsequent formation of $ZnTiO_3$. The variable temperature XRD (VT-XRD) for the same sample is shown in Fig. 8. The first evidence of reaction between ZnO and TiO_2 nano-powders prepared separately and then mixed, is reported to be at 430 °C.[57]

The TG-DTA (thermal gravimetric analysis-differential thermal analysis) of the sample (ESI†) had two crystallisation peaks in the DTA at 453 °C and 690 °C as shown on the VT-XRD (Fig. 8). The first peak correlates well with the reported data for the reaction between ZnO and TiO_2 nanopowders. The second peak at 690 °C correlates with the VT-XRD where the onset of crystalline Zn_2TiO_4 was seen. In the heat-treatment studies, Zn_2TiO_4 was reported to form around 800 °C. Most studies for the synthesis of zinc titanates from ZnO and TiO_2 powders do not heat-treat them below this temperature.[15] Yang and Swisher achieved 5% zinc orthotitanate after heating at 500 °C for 48 hours.[13] In zinc titanates made from sol–gel and heat-treatment route, where the nano-ZnO and TiO_2 mixtures reduce the diffusion length, Zn_2TiO_4 was present above 400 °C.[60] This correlates with the peaks observed herein for DTA and in the VT-XRD.

3.3 Photocatalytic activity

The as-prepared and heat-treated samples were evaluated as photocatalysts for the decolourisation of MB. Fig. 9 shows the rate of decolourisation of MB for the Ti–Zn–O binary mixtures "as-prepared" (hatched bars) and after heat-treatment (solid bars). The tests were carried out using MB and the samples were illuminated for up to a total of 6 h. Concentrations of dye remaining were measured at 30, 60 90 and 120 minutes, and then at hourly intervals. The rate was calculated assuming first order kinetics (eqn (2)) which have been shown to fit well for photodecolourisation of certain dyes including MB (in air).[61] In all cases a linear relationship was observed for $\ln(C/C_0)$ against time.

$$\ln(C/C_0) = -k't \quad (2)$$

(C = concentration at time t, C_0 = initial concentration, t = time, k' is the composite rate constant).

The combination of light with a semiconductor, leads to the promotion of redox reaction which take part on the surface of the semiconductor. In particular, the electronic structure of a photocatalyst consists of a filled valence band (VB) and the empty conduction band (CB). When the photocatalysts are irradiated with light energy greater than their bandgap (E_g), electrons are excited from the VB into CB leaving holes in the VB. The generated electron–hole pairs can (i) independently migrate to the surface to take part in redox reaction utilised for decomposition of various organic compounds, bacteria, *etc.*, (ii) be shallow or deep trapped, or (iii) recombined together to give

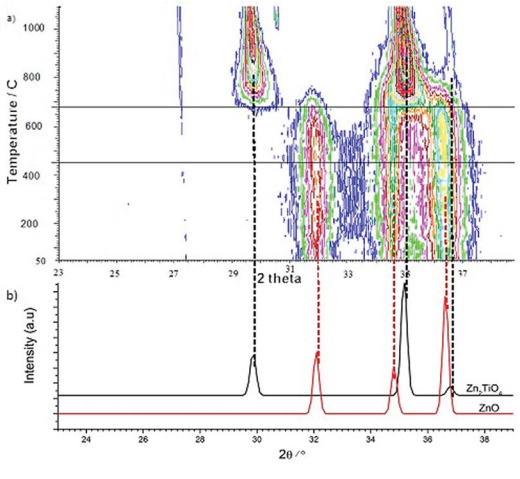

Fig. 8 (a) VT-XRD contour pattern of sample 8 being heated from 25–1100 °C in air (b) ZnO and Zn_2TiO_4 peak positions samples 13a and 8a (dashed lines are a guide to peak identities, horizontal lines indicate the position heat flow peaks in the STA plot).

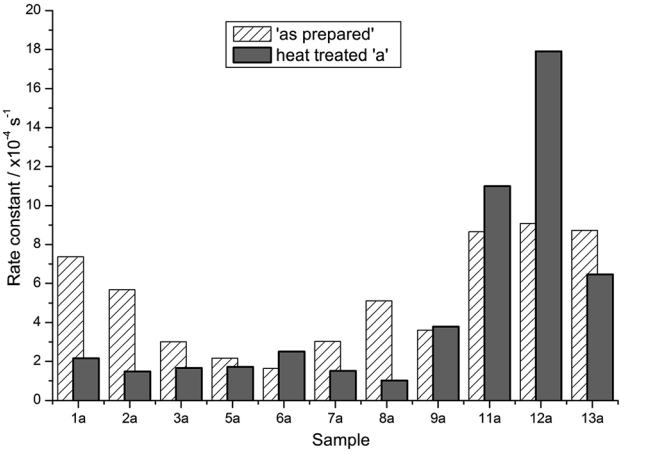

Fig. 9 First order rate constant of nanopowders (samples 1–13) for the decolourisation of MB (rate constant of as-prepared samples = hatched).

off energy in form of the heat. It is know that photocatalytic properties are dependent on certain parameters including light intensity, MB and photocatalyst concentration. Recent examples include the photocatalytic activities of ZnO catalyst doped with P were the authors reported the superior photocatalytic activity of these materials attributed to their nanocomb morphologies and increased surface defects.[62] Furthermore, ZnO–ZnS nanosheets, are known to form surface complexes, have a narrower bandgap and consequently, are photocatalytically active for the degradation of methylene blue under visible light irradiation.[63] In other cases, by utilising coupled semiconductors as in the Zn–Ti–O photocatalyst material the recombination of charge carries generated upon irradiation is decreased greatly as there is greater charge separation. This is done by the transfer of exciting electron from the conduction band of ZnO to the conduction band of TiO_2 and the transfer of the generated the hole from the valence band of TiO_2 to the valence band of ZnO, thus increasing the lifetime of the charge carriers.[2,9–11]

By comparing the diffraction patterns (Fig. 3) to the rates shown in Fig. 9 it can be seen that the samples with very low rates of decolourisation, *i.e.* samples 4 (75 : 25), 5 (70 : 30) and 6 (60 : 40) had XRD patterns containing very broad indistinct peaks, suggesting the samples with an apparent lower crystallinity had lower activity. From sample 7 (50 : 50) to 13 (0 : 100), the photocatalytic activity was amongst the highest of the as-prepared Ti–Zn–O binary nanopowder mixtures. All these samples showed a sharp transition at the bandgap with a higher UVA absorption and had a ZnO structure (as revealed from XRD patterns). The additional absorption could contribute to the higher activity. Additionally, surface oxygen deficiencies seen in the XPS spectra of samples with high Zn content (samples 8–13) can act as capture centres for photo-excited electrons and reduce recombination, enabling surface absorbed OH to form hydroxyl radicals that can take part in photocatalytic reactions.[64] The photocatalytic activity of sample 8 (40 : 60) was greater than that of sample 7, which could be due to increased crystallinity and increased UV absorbance. Samples 9 (30 : 70) and 10 (25 : 75) showed a lower activity than sample 8 and there is a corresponding reduction in the UV absorbance for these samples. For the heat-treated samples (solid bars), in most cases, a decrease in photocatalytic activity was observed in comparison to the corresponding as-prepared materials (hatched bars). The heat-treatment generally introduced a phase composition change followed by a decrease in surface area. For example, the heat-treated sample 1a was transformed from anatase to a rutile phase TiO_2 (as confirmed from XRD patterns) process of which will have caused decrease in specific surface area. Some reports have shown that rutile can be less active than anatase and its photocatalytic activity is often found to be dependent on the number of surface active sites.[2] Therefore, it is expected that a reduction in the surface area and the increase in particle size due to heating as well as the transformation to rutile will reduce the photocatalytic activity compared to the as-prepared sample.

Sample 2a–5a all exhibited lower photocatalytic activities than the corresponding as-prepared samples. This is likely to be due to the change from anatase to rutile and decreasing specific surface area. Sample 6a had a higher activity than the corresponding as-prepared sample. The as-prepared sample 6 appeared to be amorphous (as revealed from XRD data) and was expected to show an increase in crystallinity with heat-treatment (and consequently an increase in photocatalytic activity). Like samples 2a–5a, sample 6a is a mixture of rutile and $ZnTiO_3$ phase, which suggests the increased crystallinity could lead to an increase in the photocatalytic activity compared to the original sample, however, the activity is still relatively low. The activity of sample 8a (pure zinc orthotitanate) exhibited the lowest activity in comparison to all as-prepared and heat-treated samples, which suggests that Zn_2TiO_4 made *via* this method was photocatalytically inactive. However, in samples 9a–12a, which are mixtures of ZnO and Zn_2TiO_4, revealed high rates of photodecolourisation towards methylene blue. The activity of heat-treated pure ZnO sample (13a) was lower than sample 12a ($\geq$50%) and pure ZnO before heat-treatment (as-prepared sample 13). Further, a general increase in photocatalytic activity was observed from sample 9a to 12a. This coincides with the coupling of Zn_2TiO_4 and ZnO phases, possibly giving enhanced electron–hole separation as a consequence of the two different phases. Additionally, the UV-Vis absorption profiles of samples 8a–12a were similar in appearance to those for sample 13 and 13a (ZnO like). The bandgap values were between 3.22–3.24 eV assuming a direct transitions (see ESI†). The exact positions of the conduction and valence band are as yet undetermined but they may allow efficient charge transfer between the two intimately mixed materials that suppresses recombination.

4. Conclusions

A continuous hydrothermal flow synthesis method was successfully used for the synthesis of mixtures of (anatase) and ZnO (wurtzite) nanomaterials directly in a single step method. By varying the precursor ratios in the CHFS system, a wide range of compositions including solid solutions were accessed directly. A high resolution powder diffraction facility at Diamond was employed to obtain high – quality data in a rapid and time efficient manner. The CHFS approach enabled the production of complete range of Ti–Zn oxide nanomaterials in a rapid manner with particle size ranging from 66 nm (ZnO) to 4.9 nm (TiO_2), all of which generally exhibited high surface areas. Additionally, a high solid solubility of up to *ca.* 25% of Zn in the anatase lattice was observed for the as-prepared nanomaterials. The transition from anatase to wurtzite as the main phase is also seen in changes in the bandgap and BET surface area values. The as-prepared Ti–Zn–O binary nanopowders all displayed an 'averaged' bandgap value between that of TiO_2 and ZnO. The UV absorption profiles gradually varied across the samples and the as-prepared sample containing Ti : Zn ratio of 40 : 60 displayed better broad spectrum of UVA and UVB absorption. The intimately mixed of Ti–Zn–O nanopowders produced by CHFS were heat-treated to form zinc titanates. The photocatalytic activity varied with the Ti : Zn ratio and highest photocatalytic activities in the as-prepared samples were found for the pure crystalline anatase and zinc oxide structures. The

photoactivity also varied depending on the crystallinity and the absorbance as well as the structure and surface area. For the heat-treated powders, the ZnO and Zn_2TiO_3 mixtures displayed high activity, which may be of interest for UV photocatalysis applications. The highest activity was observed when the as-prepared sample containing a Ti : Zn ratio of *ca.* 10 : 90 that was heat-treated to form a phase mixture of ZnO and Zn_2TiO_4. In conclusion, the CHFS route allowed the production of nanomaterials with improved particle properties, such as small particle size, high surface area, high crystallinity and with unusual phase stability in addition to tunable optical properties.

Acknowledgements

EPSRC is thanked for funding the High Throughput Nanoceramics Discovery project [JAD, EPSRC grant ref. EP/D038499/1]. Sun Chemical (JG) is also thanked for supporting industrial CASE award. This work was supported in part (JCK) by WCU Program through the National Research Foundation of Korea (NRF) funded by the Ministry of Education, Science and Technology (no. R31-10069). Professor D. Cockayne, Drs L. Karlsson, J. Hutchinson and C. Hetherington at Oxford Department of Materials are thanked for assistance and access to the HR-TEM instrument (under the EPSRC access scheme grant reference: EP/F01919X/1). Nicola Mordan at the Eastman Dental institute London is thanked for her assistance with EDX analysis. Ignacio Villar and Emily Smith from the University of Nottingham (EPSRC grant EP/F019750/1) are thanked for assistance and access to the XPS instrument.

Notes and references

1 M. A. Fox and M. T. Dulay, *Chem. Rev.*, 1993, **93**(1), 341.
2 O. Carp, C. L. Huisman and A. Reller, *Prog. Solid State Chem.*, 2004, **32**(1–2), 33.
3 P. Kullavanijaya and H. W. Lim, *J. Am. Acad. Dermatol.*, 2005, **52**(6), 937.
4 S. B. Levy, *Dermatol. Ther.*, 1997, **4**(59), 59.
5 D. C. Look, *Mater. Sci. Eng., B*, 2001, **80**(1–3), 383.
6 V. P. S. Judin, *Chem. Br.*, 1993, **29**(6), 503.
7 N. Serpone, D. Dondi and A. Albini, *Inorg. Chim. Acta*, 2007, **360**(3), 794.
8 Ü. Özgür, Y. Alivov, C. Liu, A. Teke, M. A. Reshchikov, S. Doğan, V. Avrutin, S. J. Cho and H. Morkoç, *J. Appl. Phys.*, 2005, **98**, 041301.
9 W. Y. Choi, A. Termin and M. R. Hoffmann, *J. Phys. Chem.*, 1994, **98**(51), 13669.
10 T. L. Thompson and J. T. Yates, *Top. Catal.*, 2005, **35**(3–4), 197.
11 D. Chen, H. Zhang, S. Hu and J. H. Li, *J. Phys. Chem. C*, 2008, **112**(1), 117.
12 A. Nasu and Y. Otsubo, *J. Colloid Interface Sci.*, 2007, **310**(2), 617.
13 J. Yang and J. H. Swisher, *Mater. Charact.*, 1996, **37**(2–3), 153.
14 P. M. Botta, E. F. Aglietti and J. M. P. Lopez, *J. Mater. Sci.*, 2004, **39**(16–17), 5195.
15 C. F. Shih, W. M. Li, M. M. Lin, K. T. Hong, C. Y. Hsiao and C. L. Lee, *Electrochem. Solid-State Lett.*, 2008, **11**(12), K105.
16 Y. S. Chang, Y. H. Chang, I. G. Chen, G. J. Chen and Y. L. Chai, *J. Cryst. Growth*, 2002, **243**(2), 319.
17 F. H. Dulin and D. E. Rase, *J. Am. Ceram. Soc.*, 1960, **43**, 125–131.
18 R. S. Mane, W. J. Lee, H. M. Pathan and S. H. Han, *J. Phys. Chem. B*, 2005, **109**(51), 24254.
19 H. Y. Lin, Y. Y. Chou, C. L. Cheng and Y. F. Chen, *Opt. Express*, 2007, **15**(21), 13832.
20 D. Barreca, E. Comini, A. P. Ferrucci, A. Gasparotto, C. Maccato, C. Maragno, G. Sberveglieri and E. Tondello, *Chem. Mater.*, 2007, **19**(23), 5642.
21 S. S. Lin, J. L. Huang and P. Sajgalik, *Surf. Coat. Technol.*, 2005, **191**(2–3), 286.
22 A. A. Dakhel, *Appl. Phys. A: Mater. Sci. Process.*, 2003, **77**(5), 677.
23 B. L. Zhu, C. S. Xie, W. Y. Wang, K. J. Huang and J. H. Hu, *Mater. Lett.*, 2004, **58**(5), 624.
24 G. Marci, V. Augugliaro, M. J. Lopez-Munoz, C. Martin, L. Palmisano, V. Rives, M. Schiavello, R. J. D. Tilley and A. M. Venezia, *J. Phys. Chem. B*, 2001, **105**(5), 1026.
25 P. Boldrin, A. K. Hebb, A. A. Chaudhry, L. Otley, B. Thiebaut, P. Bishop and J. A. Darr, *Ind. Eng. Chem. Res.*, 2007, **46**(14), 4830.
26 A. A. Chaudhry, S. Haque, S. Kellici, P. Boldrin, I. Rehman, A. K. Fazal and J. A. Darr, *Chem. Commun.*, 2006, **21**, 2286–2288.
27 J. A. Darr and M. Poliakoff, *Chem. Rev.*, 1999, **99**, 495.
28 X. L. Weng, P. Boldrin, I. Abrahams, S. Skinner and J. A. Darr, *Chem. Mater.*, 2007, **19**(18), 4382.
29 X. L. Weng, P. Boldrin, I. Abrahams, S. J. Skinner, S. Kellici and J. A. Darr, *J. Solid State Chem.*, 2008, **181**(5), 1123.
30 Z. C. Zhang, S. Brown, J. B. M. Goodall, X. L. Weng, K. Thompson, K. N. Gong, S. Kellici, R. J. H. Clark, J. R. G. Evans and J. A. Darr, *J. Alloys Compound.*, 2009, **476**(1–2), 451.
31 Z. Zhang, J. B. Goodall, S. Brown, L. Karlsson, R. J. Clark, J. L. Hutchison, I. U. Rehman and J. A. Darr, *Dalton Trans.*, 2010, **39**(3), 711.
32 T. Lin, S. Kellici, K. Gong, K. Thompson, J. R. G. Evans, X. Wang and J. A. Darr, *J. Comb. Chem.*, 2010, **12**(3), 383.
33 C. J. Tighe, R. Q. Cabrera, R. I. Gruar and J. A. Darr, *Ind. Eng. Chem. Res.*, 2013, **52**(16), 5522.
34 R. I. Gruar, C. J. Tighe and J. A. Darr, *Ind. Eng. Chem. Res.*, 2013, **52**(15), 5270.
35 R. Quesada-Cabrera, X. Weng, G. Hyett, R. J. H. Clark, X. Z. Wang and J. A. Darr, *ACS Comb. Sci.*, 2013, **15**(9), 458.
36 S. Ohara, T. Mousavand, M. Umetsu, S. Takami, T. Adschiri, Y. Kuroki and M. Takata, *Solid State Ionics*, 2004, **172**(1), 261.
37 K. Sue, K. Kimura and K. Arai, *Mater. Lett.*, 2004, **58**(25), 3229.
38 T. Adschiri, K. Kanazawa and K. Arai, *J. Am. Ceram. Soc.*, 1992, **75**(4), 1019.
39 N. Millot, B. Xin, C. Pighini and D. Aymes, *J. Eur. Ceram. Soc.*, 2005, **25**(12), 2013.

40 R. Viswanathan, G. D. Lilly, W. F. Gale and R. B. Gupta, *Ind. Eng. Chem. Res.*, 2003, **42**(22), 5535.
41 S. Kellici, K. Gong, T. Lin, S. Brown, R. J. H. Clark, M. Vickers, J. K. Cockcroft, V. Middelkoop, P. Barnes, J. M. Perkins, C. J. Tighe and J. A. Darr, *Philos. Trans. R. Soc., A*, 2010, **368**(1927), 4331.
42 X. Weng, J. K. Cockcroft, G. Hyett, M. Vickers, P. Boldrin, C. C. Tang, S. P. Thompson, J. E. Parker, J. C. Knowles, I. Rehman, I. Parkin, J. R. Evans and J. A. Darr, *J. Comb. Chem.*, 2009, **11**(5), 829.
43 P. Kubelka and F. Munk, *Zeit. Für Tekn. Physik*, 1931, **12**, 593.
44 K. Thompson, J. Goodall, S. Kellici, J. A. Mattinson, T. A. Egerton, I. Rehman and J. A. Darr, *J. Chem. Technol. Biotechnol.*, 2009, **84**(11), 1717.
45 A. Mills and J. S. Wang, *J. Photochem. Photobiol., A*, 1999, **127**(1–3), 123.
46 S. P. Qiu and S. J. Kalita, *Mater. Sci. Eng., A*, 2006, **435**, 327.
47 Y. Deng, G. S. Wang, N. Li and L. Guo, *J. Lumin.*, 2009, **129**(1), 55.
48 C. Q. Xia, Y. Gu and F. H. Zeng, *J. Cent. South Univ. Technol.*, 2003, **10**(2), 87.
49 T. J. Chen and P. Y. Shen, *J. Phys. Chem. C*, 2009, **113**(1), 328.
50 Z. M. Shi and L. N. Jin, *J. Non-Cryst. Solids*, 2009, **355**(3), 213.
51 (*a*) W. J. Zhang, S. L. Zhu, Y. Li and F. H. Wang, *Vacuum*, 2007, **82**(3), 328; (*b*) C. T. Wang and J. C. Lin, *Appl. Surf. Sci.*, 2008, **254**(15), 4500.
52 Z. Zhang, J. B. M. Goodall, D. J. Morgan, S. Brown, R. J. H. Clark, J. C. Knowles, N. J. Mordan, J. R. G. Evans, A. F. Carley, M. Bowker and J. A. Darr, *J. Eur. Ceram. Soc.*, 2009, **29**(11), 2343.
53 C. D. Wagner, A. V. Naumkin, A. Kraut-Vass, J. W. Allison, C. J. Powell and J. R. J. Rumble, *NIST database*, http://srdata.nist.gov/xps/, 2003.
54 Z. L. Liu, B. Guo, L. Hong and H. X. Jiang, *J. Phys. Chem. Solids*, 2005, **66**(1), 161.
55 C. T. Wang and J. C. Lin, *Appl. Surf. Sci.*, 2008, **254**(15), 4500–4507.
56 H. T. Cao, Z. L. Pei, J. Gong, C. Sun, R. F. Huang and L. S. Wen, *J. Solid State Chem.*, 2004, **177**(4–5), 1480.
57 L. Q. Jing, B. Q. Wang, B. F. Xin, S. D. Li, K. Y. Shi, W. M. Cai and H. G. Fu, *J. Solid State Chem.*, 2004, **177**(11), 4221.
58 M. Chen, X. Wang, Y. H. Yu, Z. L. Pei Bai, X. D. Sun, R. F. Huang and L. S. Wen, *Appl. Surf. Sci.*, 2000, **158**(1–2), 134.
59 H. T. Kim, Y. Kim, M. Valant and D. Suvorov, *J. Am. Ceram. Soc.*, 2001, **84**(5), 1081.
60 S. A. Mayen-Hernandez, G. Torres-Delgado, R. Castanedo-Perez, J. M. Marin, M. Gutierrez-Villarreal and O. Zelaya-Angel, *Sol. Energy Mater. Sol. Cells*, 2007, **91**(15–16), 1454.
61 C. H. Wu and J. M. Chern, *Ind. Eng. Chem. Res.*, 2006, **45**(19), 6450.
62 S. Xie, Y. Liu, Z. Chen, X. Chen and X. Wang, *RSC Adv.*, 2013, **3**, 26080.
63 A. K. Kole, C. S. Tiwary and P. Kumbhakar, *CrystEngComm*, 2013, **15**, 5515.
64 L. Q. Jing, Z. L. Xu, X. J. Sun, J. Shang and W. M. Cai, *Appl. Surf. Sci.*, 2001, **180**, 308.